

Neural 3D Object Reconstruction with Small-Scale Unmanned Aerial Vehicles

Álmos Veres-Vitályos, Genis Castillo Gomez-Raya, Filip Lemic*, Daniel Johannes Bugelnig, Bernhard Rinner, Sergi Abadal, Xavier Costa-Pérez

Abstract—Small Unmanned Aerial Vehicles (UAVs) exhibit immense potential for navigating indoor and hard-to-reach areas, yet their significant constraints in payload and autonomy have largely prevented their use for complex tasks like high-quality 3-Dimensional (3D) reconstruction. To overcome this challenge, we introduce a novel system architecture that enables fully autonomous, high-fidelity 3D scanning of static objects using UAVs weighing under 100 grams. Our core innovation lies in a dual-reconstruction pipeline that creates a real-time feedback loop between data capture and flight control. A near-real-time (near-RT) process uses Structure from Motion (SfM) to generate an instantaneous pointcloud of the object. The system analyzes the model quality on the fly and dynamically adapts the UAV’s trajectory to intelligently capture new images of poorly covered areas. This ensures comprehensive data acquisition. For the final, detailed output, a non-real-time (non-RT) pipeline employs a Neural Radiance Fields (NeRF)-based Neural 3D Reconstruction (N3DR) approach, fusing SfM-derived camera poses with precise Ultra Wide-Band (UWB) location data to achieve superior accuracy. We implemented and validated this architecture using Crazyflie 2.1 UAVs. Our experiments, conducted in both single- and multi-UAV configurations, conclusively show that dynamic trajectory adaptation consistently improves reconstruction quality over static flight paths. This work demonstrates a scalable and autonomous solution that unlocks the potential of miniaturized UAVs for fine-grained 3D reconstruction in constrained environments, a capability previously limited to much larger platforms.

I. INTRODUCTION

Recent advances in robotics resulted in an uptake of Unmanned Aerial Vehicles (UAVs) [1], [2]. Additionally, developments in device miniaturization have driven the creation of advanced systems such as small UAVs. The development of these small UAVs, typically weighing less than a kilogram, has been enabled by the miniaturization and cost reduction of electronic components (micro-processors, sensors, batteries, and wireless communication units) [3]. Small UAVs are opening new avenues for applications such as structural monitoring automation [4], generation of Virtual Reality (VR) content [5], quality control [6], cultural heritage preservation [7], geology [8], and more. These UAVs are primarily envisioned for indoor use, which reduces the need for flight

licenses and makes them more appealing for broader market adoption. However, none of today’s commercial small UAVs offer sufficient autonomy to navigate without skilled human supervision, which limits the scalability of their missions [3]. This limitation arises because the flight is particularly energy-intensive, especially for small UAVs. As their size decreases, critical scaling issues emerge, such as lower power density in motors, reduced transmission efficiency, and increased energy consumption in maneuvers like hovering [9]. These constraints lead to severe limitations in flight autonomy, path planning, battery endurance, and payload capability, which fundamentally hinder the UAV’s ability to perform more complex tasks.

One particularly compelling application of small UAVs is the autonomous 3-Dimensional (3D) reconstruction of static objects [10] which is useful for various domains, including industry [11], urban monitoring [12], disaster management [13], warehouse operations [14], subterranean explorations [15], heritage documentation [16], and VR [17]. While smartphones and handheld devices have enabled progress in 3D reconstruction, they require manual intervention and cannot be fully automated, which limits their scalability.

In this paper, we show that such applications can be enabled and automated by small UAVs. Specifically, we introduce a system architecture for small UAV-supported autonomous generation of accurate 3D digital representations of static objects. In our architecture, small UAVs carry camera sensors and act as their power source. Each UAV visits a set of locations around the object, hovers, captures images, and transmits them wirelessly to a station running an open-source pipeline for generating a 3D object representation. The proposed architecture leverages near-real-time (RT) reconstruction to enable features like adaptive UAV path planning. The system also incorporates Neural Radiance Fields (NeRF), a novel Neural 3D Reconstruction (N3DR) approach for highly accurate 3D reconstruction and volumetric rendering.

The key technological innovation of the system lies in its use of small UAVs weighing under 100 grams, demonstrating how advanced functionality can still be achieved despite the inherent constraints of such lightweight platforms. This is particularly significant due to its ability to enable small-scale, autonomous 3D reconstruction in unknown, complex, indoor, and hard-to-reach environments. The main scientific innovation of the system stems from its novel integration of near-RT 3D reconstruction with dynamic UAV positioning. This approach is relevant because it enables the UAV to adapt its trajectory based on the quality of ongoing spatial reconstruction. By leveraging this awareness, the system can intelligently adjust the UAV’s path for more accurate reconstructions, pushing

*Corresponding author.

Á. Veres-Vitályos, G. Castillo, F. Lemic, and X. Costa-Pérez are affiliated with i2CAT Foundation, Spain, email: {name.surname}@i2cat.net.

D. Bugelnig and B. Rinner are affiliated with University of Klagenfurt, Austria, email: {name.surname}@aau.at.

S. Abadal is affiliated with Universitat Politècnica de Catalunya, Spain, email: abadal@ac.upc.edu.

F. Lemic is also affiliated with the Faculty of Electrical Engineering and Computing, University of Zagreb, Croatia.

X. Costa-Pérez is also affiliated with NEC Labs Europe GmbH, Germany and ICREA, Spain.

the boundaries of autonomous UAV-based 3D reconstruction. Furthermore, the N3DR system offers precise rendering of the object on top of the near-RT support, which not only improves reconstruction accuracy but also demonstrates how real-time feedback can enhance robotic path planning for 3D object representation.

The architecture has been prototypically implemented using off-the-shelf Crazyflie UAVs, Structure from Motion (SfM) and Nerfacto from Nerfstudio for near-RT and non-RT 3D reconstruction, respectively. Experimental characterization of the prototype yielded promising results regarding 3D reconstruction performance. Our system combines compact hardware and lightweight software with near-RT pointcloud generation, making it suitable for autonomous 3D reconstruction of small objects in indoor and hard-to-reach areas, where collision avoidance and multi-UAV coordination are critical. Compared to existing literature, which typically focuses on larger UAVs and larger objects (cf., Figure 1), our approach opens new possibilities for fine-grained 3D reconstruction of small, static objects in constrained environments.

This paper is structured as follows. In Section II, we review the related work in the field of UAV-based 3D reconstruction and small UAV applications. Section III presents the proposed system architecture, detailing the key components and their interactions. In Section IV, we describe the system implementation, including hardware setup and software pipelines for 3D object reconstruction. Section V presents the evaluation methodology, outlining the experimental setup and performance metrics used. In Section VI, we provide the results of the experiments, including both qualitative and quantitative analyses of the 3D reconstruction performance. Section VII discusses the findings, and presents directions for future work. The work is concluded in Section VIII.

II. RELATED WORKS

A. 3D Reconstruction of Static Objects

Photogrammetry is a technique that extracts 3D shape information from physical objects [18]. Despite originating in 1867, it remains one of the most widely used methods for 3D object reconstruction. It is applied across various fields, including topographic mapping, archaeology, architecture, infrastructure inspection, and VR content generation [19].

Photogrammetry uses two primary data sources: images and Light Detection and Ranging (LiDAR) scans [19]. LiDAR is a sensing method that employs laser light to measure distances and create precise 3D representations of objects or surfaces. It excels in generating point clouds by combining depth data with Red, Green and Blue (RGB) imagery. However, LiDAR systems are often too large and heavy to be deployed on small UAVs, making them impractical for applications where size and weight are critical constraints, such as in indoor environments or with small UAV platforms.

In contrast, image-based 3D reconstruction offers several advantages for small-scale UAV applications, including lower cost, energy efficiency, and the ability to capture high-resolution textures. One of the most popular image-based methods is SfM, which reconstructs 3D structures from overlapping 2D images by identifying matching features across

them and estimating camera positions [20]. SfM is widely used due to its robustness and ability to handle large datasets, though it can be computationally intensive, particularly during feature matching and optimization stages.

Recent advances in machine learning have further pushed the boundaries of 3D reconstruction, particularly with techniques like NeRF [21], [22], which use neural networks to synthesize novel views of a scene by optimizing a volumetric scene representation. NeRF is capable of producing high-quality, detailed reconstructions, but its computational requirements can be prohibitive for real-time applications. Gaussian Splatting (GS) [23] offers a more efficient alternative by approximating the scene with Gaussian functions, enabling faster rendering while maintaining competitive detail levels. Another breakthrough technique is Instant Neural Graphics Primitives (instant-npg), which leverages a multi-resolution hash table to rapidly reconstruct 3D scenes [24], providing near-instantaneous results suitable for near-RT applications.

We use Nerfacto [25], a NeRF-based N3DR implementation, due to its balance between quality and computational feasibility. This choice is supported by our prior work [26], where we experimentally compared Nerfacto with alternatives like instant-npg [24] and Splatfacto [27] on UAV-captured datasets. The results showed that Nerfacto consistently achieved more accurate and stable reconstructions under the resource and noise constraints of small UAV platforms. While this work does not aim to optimize its hyperparameters, it demonstrates the feasibility of small UAV-based 3D reconstruction using Nerfacto.

B. UAV-based 3D Object Reconstruction

UAVs have gained increasing attention for their ability to enable applications across transportation, surveillance, search and rescue, disaster management, and remote immersion through mobile VR [28]. The UAV market is expected to grow from \$19.3 billion in 2019 to \$45.8 billion by 2025, with a Compound Annual Growth Rate (CAGR) of 15.5% [28], reflecting their growing impact in various domains.

UAV-supported 3D digital reconstruction of physical objects is the application of interest in this work, which draws inspiration from the existing literature. The majority of the works target metropolitan area (MA)-sized objects and primarily outdoor environments. For example, an embedded near-RT UAV system for 3D scene reconstruction is proposed in [29]. The UAV system features a DJI F550 hexacopter frame, a 3DR pixhawk autopilot equipped with GPS and compass, a 915 MHz telemetry radio to the ground station computer, a FrSky receiver, a Spectrum DX7 transmitter, a Tarot brushless gimbal, and 3 cell LIPO batteries which sustain 20 min long flights. The total weight of the system has not been reported, however the reported maximum payload of 1 kg is indicative of a substantially large system. The physical object of interest in [29] is an outdoor scene, in particular a tree. In [30], the authors focus on 3D digital reconstruction of outdoor scenery such as houses and parking lots. For enabling this application, they utilize DJI Mavic Pro 2 weighting 907 g, equipped with a 12 Mpx Hasselblad camera. Moreover, the authors

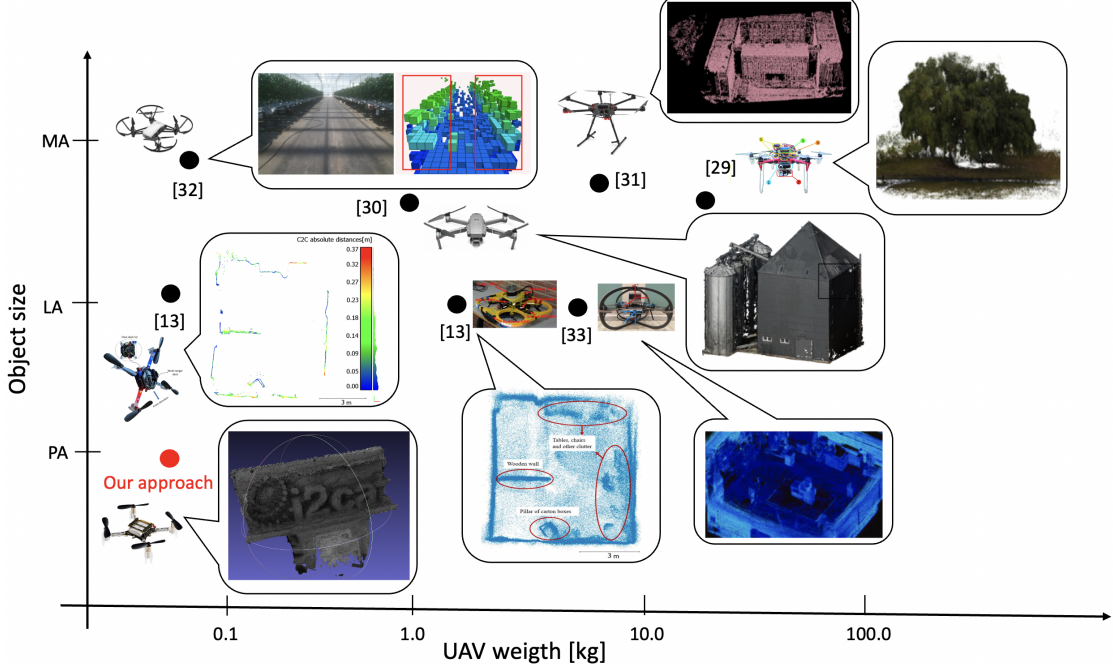


Fig. 1: Positioning of the proposed system with regard to the state-of-the-art along two dimensions: UAV weight (Kg) vs Object size (MA: metropolitan area, LA: large area, PA: personal area).

in [31] propose a UAV-based system for indoor precision agriculture applications such as stock or crop monitoring. In the prototypical implementation of their system, they utilize a DJI Tello UAV weighing approximately 80 g, and focus on an entire indoor farm as the physical object of interest. In [32], a DJI M600 Pro UAV-based setup with the weight of roughly 9.5 kg enhanced with NVIDIA Jetson TX2 is proposed for 3D reconstruction of buildings.

Some literature works target indoor large area (LA) objects. For example, in [13] a MAX UAV-based system for indoor environment mapping is proposed. The overall weight of the UAV system is 3172 g, while the physical object of interest is an indoor environment, as indicated in Figure 1. In addition, the authors enable the same application using the Crazyflie UAV comparable to the ones utilized in this work, however aiming at rather rudimentary accuracy of 3D object reconstruction, as indicated in the figure. Finally, an autonomous UAV-based system for indoor scene reconstruction is proposed in [33]. The UAV utilized for 3D object reconstruction targets indoor sites such as residences, features the weight of 1.45 kg [15], and is further enhanced with LiDAR and stereo camera sensors, among others.

Our proposed system differs from existing literature by utilizing small-scale Crazyflie UAVs (weighing less than 100 g) to reconstruct smaller, personal area (PA)-sized objects with high precision. This is a significant distinction, as most works focus on larger UAVs or outdoor environments, which do not face the same energy and scaling limitations (cf., Figure 1). Moreover, the proposed system integrates near-RT 3D reconstruction with dynamic UAV path planning, which enables more accurate, adaptive image capture based on the quality of the ongoing reconstruction. Unlike existing works, which primarily rely on manual or semi-automated control,

this system demonstrates a fully autonomous and scalable solution for small object reconstruction indoors. Finally, while previous efforts primarily employ traditional reconstruction techniques or large UAV platforms, this work combines small UAVs with advanced N3DR techniques like Nerfacto for high-quality volumetric rendering. The focus on location-aware 3D reconstruction and UAV dynamic positioning based on spatial quality differentiates this work from earlier efforts that lack such integration.

III. SYSTEM ARCHITECTURE

Figure 2 depicts our system architecture for generating 3D object representations. The architecture consists of three components: the multi-UAV setup with UWB-based positioning and the base station containing the near-RT and non-RT generation pipelines.

The multi-UAV setup consists of UAVs equipped with onboard camera sensors and a UWB positioning system for precise localization in (indoor) environments. The UAVs circle the object along fixed waypoints, capture images from various angles, and transfer images with location data to the base station. The base station can adapt the trajectory by sending new locations to the UAVs. The near-RT generation component processes the images received from the UAVs in real time. The images are preprocessed and merged into a rough 3D model of the object (instantaneous pointcloud), which is used to estimate the coverage level of the object, enabling the UAVs to dynamically adjust their positions to improve the reconstruction quality. Finally, the non-RT reconstruction component creates the high-fidelity 3D model using non-RT techniques. This process takes advantage of the data gathered during the near-RT processing and employs advanced methods like NeRFs to produce highly detailed volumetric rendering.

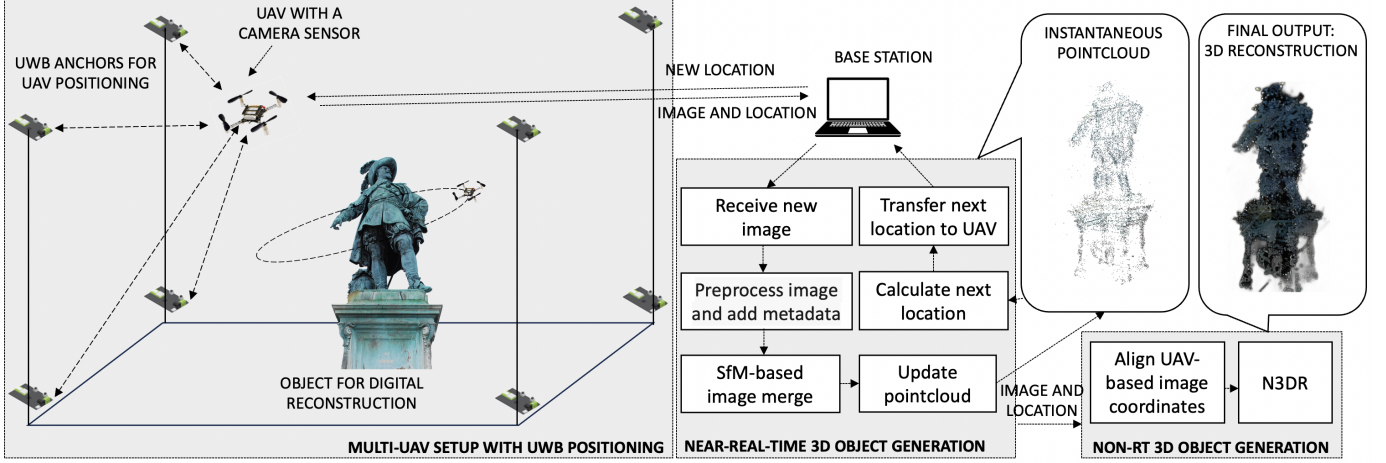


Fig. 2: Our system architecture for small UAV-supported generation of 3D objects representations composed by a UAV with UWB positioning and a base station executing near-RT and non-RT 3D object generation. The UAVs circle around the object and transfer images from predefined locations to the base station. The images are merged to an instantaneous pointcloud in near-RT and together with location data to the 3D reconstruction in not-RT. The current coverage level of the object is estimated with the instantaneous pointcloud, and a new location to a section with insufficient coverage is sent to the UAV (dynamic trajectory adaptation).

Our system is initialized with the waypoints of the initial circles around the object, and the UAVs need to face the object before take-off. To initiate 3D reconstruction, the base station triggers the take-off and movement to the initial location. The UAVs then follow to the predefined or dynamically computed locations depending on whether static or dynamic trajectories have been selected. If no further locations are provided, the reconstruction mission is completed, and the UAVs descend for landing. Our system can handle a variable number of UAVs, and in this paper we present results with one and two UAVs.

Two images taken at different locations are needed for producing the initial representation, hence the UAV is initially instructed to take two images of the object directly in front of it, with a slight drift in the locations. The pointcloud can then be generated using some of existing near-RT reconstruction approaches, such as the well-known SfM algorithm [34]. The SfM algorithm operates on the principle of obtaining the location and orientation of a camera with respect to an object, based on which it is able to reconstruct the object.

The images are complemented by metadata information containing the camera parameters (i.e., focal length, sensor size, image size, camera serial number), which are later used for 3D reconstruction. The images are further preprocessed, for example, by removing the background, applying a sharpening filter, or adjusting the brightness. This image processing depends on the particular application to increase the effectiveness of feature detection in images and the accuracy of the estimated camera positions.

Each metadata-annotated and preprocessed image is then sequentially utilized in a pipeline for near-RT 3D reconstruction. The key steps consist of obtaining the intrinsic camera parameters (from image metadata), feature extraction and matching, and applying SfM [34]. During the process, the camera positions and poses for each image are estimated based on the camera intrinsic parameters, which is easy to utilize for the reconstruction, yet it could feature low estimation accuracy especially for low-quality images taken by small UAVs.

A. Dynamic UAV Trajectory Adaptation

Each UAV can follow the predefined, static trajectory for capturing images of the object. However, the near-RT reconstruction capabilities also allow for dynamic adaptation of the UAV's trajectory based on the current quality of the reconstructed object.

The dynamic trajectory adaptation aims to guide the UAV towards viewpoints that improve the reconstruction quality of insufficiently covered object areas, while avoiding redundant image capture. To achieve this, the UAV's circular flight path around the object is divided into slices, which are fixed angular segments defined by the UAV's yaw orientation. Each slice corresponds to a specific viewing direction towards the object and serves as the basic unit for coverage evaluation. In our terminology, a region is a broader area of interest, comprising one or multiple slices.

After each image capture, a near-RT SfM process generates an updated pointcloud of the object. The resulting points are preprocessed to remove background and noise. This is done by retaining only points within a predefined distance range from the estimated object centroid. The filtered set is then grouped into clusters based on spatial proximity using a Euclidean distance threshold. For each slice, the cluster that is most relevant to the intended viewpoint (i.e., located in the visible part of the object from that slice's perspective) is identified.

The reconstruction quality of a slice is quantified using a coverage score, computed as the number of points in this cluster. This score serves as a proxy for detail density and surface completeness. A slice is considered sufficiently covered if its coverage score exceeds an empirically determined threshold, chosen to ensure adequate reconstruction detail while minimising unnecessary data capture. If the coverage score is below the threshold, the slice is marked as requiring additional images.

The selection of the UAV's next position is then performed by scanning all slices for those marked as under-covered. The

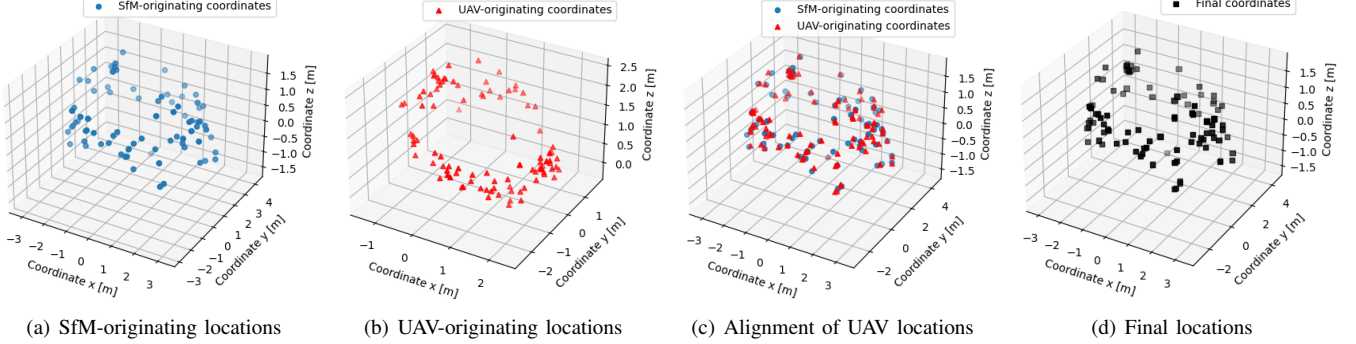


Fig. 3: Alignment of SfM- and UAV-originating image locations illustrated for a representative experiment using static, circular trajectories around the object. The depicted camera positions obtained through SfM (a) are generated by default in the reconstruction process. The positions obtained from the UAV positioning system (b) are jointly utilized with the SfM-derived positions in the location-aware non-RT reconstruction. This integration (c) involves appropriate scaling, rotation, and alignment to ensure consistency between the two coordinate frames before serving as input to the N3DR model (d).

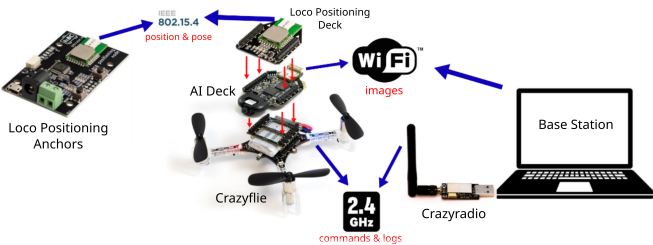


Fig. 4: Hardware components and communication interfaces of the implemented system architecture.

next waypoint is set to the geometric center of one such slice, maintaining a constant flight radius and altitude, and orienting the UAV towards the object’s centroid. This process is repeated after each reconstruction update, enabling the UAV to adapt its trajectory in real time towards viewpoints that most improve overall 3D model completeness.

B. Location-aware Non-RT 3D Reconstruction with N3DR

A photogrammetry pipeline is used for obtaining the camera intrinsic parameters from image metadata, feature extraction and matching, and SfM [34]. In this process, the camera positions and poses for each image are estimated with the intrinsic camera parameters. A N3DR-powered approach is then applied for the 3D reconstruction, e.g., with primary candidates coming from the NeRF family.

It should be noted that the estimation and tracking of UAV locations are needed for their control. This information, although not exact, is used in addition to the corresponding locations obtained through the near-RT photogrammetry pipeline, as shown in Figure 3. For optimizing the reconstruction accuracy, we can utilize these freely available UAV coordinates in addition to the ones stemming from the near-RT photogrammetry pipeline, which is expected to reduce the errors in the estimated locations of the UAV at the time of taking each image. The by-design advantage of the proposed method utilizing location-awareness comes from the fact that the integration of the cameras with the UAVs can be done at an arbitrary location (nb., often these UAVs feature multiple

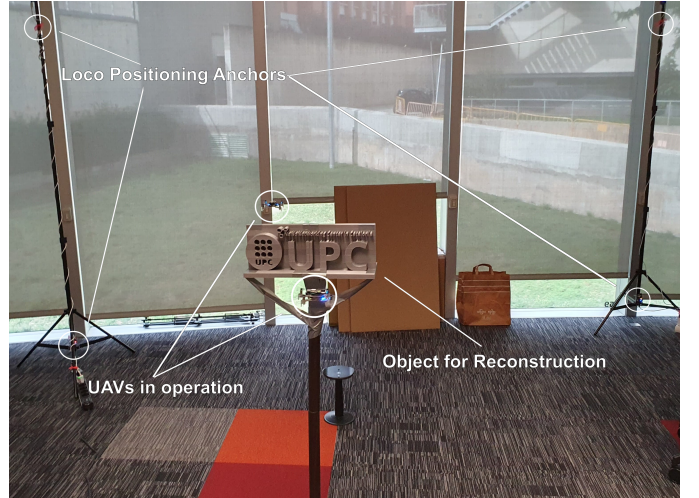


Fig. 5: Deployment in an indoor laboratory setting showing the object for reconstruction, two flying Crazyfly UAVs, and the positioning anchors.

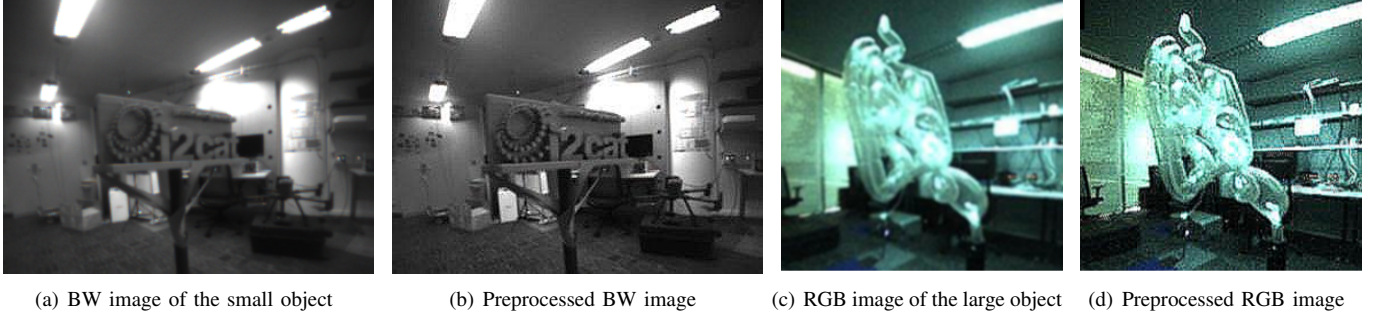
expansion boards) and does not require the calibration or hard-coding of the cameras’ locations, as long as their positioning is consistent across all UAVs in the fleet.

IV. SYSTEM IMPLEMENTATION

A. Multi-UAV Setup with UWB Positioning

Figure 4 depicts the selected hardware components for the implementation of our proposed architecture. We use Crazyfly 2.1 UAVs equipped with a proprietary Crazyradio dongle operating at the 2.4 GHz ISM band for control communication with the base station. The captured images are transferred to the base station using the integrated GAP8 CPU and the WiFi module. We use the Loco Positioning System (LPS) for UAV localization which operates in Time Difference of Arrival (TDoA) mode where each UAV estimates its position relative to fixed anchors. The measured distances are Kalman filtered by the onboard STM32 microcontroller to improve the positioning.

Each Crazyfly is equipped with an AI-Deck module hosting a GAP8 processor for efficient image processing, an ultra-low-



(a) BW image of the small object (b) Preprocessed BW image (c) RGB image of the large object (d) Preprocessed RGB image

Fig. 6: Preprocessing examples for BW and RGB images, applied in both near- and non-RT reconstructions.

power camera (320×320 pixels), and an ESP32 Wi-Fi module. Integration of the AI-Deck posed several communication challenges, particularly with the simultaneous operation of the LPS. Since both modules use the same I/O pins on the expansion connectors, hardware and firmware modifications were necessary to ensure compatibility and concurrent operation. Figure 5 shows the deployed system in our laboratory. The system can be operated with a single or multiple UAVs.

B. Near-RT 3D Object Generation Pipeline

The trajectory planning for each Crazyflie involves circling the object at a predetermined distance, either following a static trajectory based on predefined coordinates or dynamically adjusting the flight trajectory based on near-RT feedback, as outlined in the proposed system architecture. The LPS provides accurate positional data, which is crucial for maintaining the desired flight path and ensuring consistent coverage of the object from multiple angles.

The near-RT processing pipeline starts with the reception of images from the UAVs. Regardless of the object and camera type, the images are preprocessed by a sharpening filter and brightness correction to enhance visual features and contrast (cf., Figure 6). Specifically, the *Unsharp Masking* and high-pass filters were used for sharpening to improve edge definition and fine details. For contrast enhancement, *Histogram Equalization* and *Gamma Correction* were employed to adjust brightness and improve visibility. These methods were selected empirically based on their effectiveness in the given context, although additional optimizations are expected to further refine image quality.

Images are then merged on the UAV's yaw and timestamp, ensuring coherent reconstruction of the object's surface and structure. Centroid-based spatial clustering is employed to enhance reconstruction accuracy, leveraging pointcloud density to refine the 3D model. This approach mitigates irregularities caused by flight dynamics and environmental factors, producing a relatively detailed and accurate object representation as output of the update pointcloud step.

Dynamic trajectory adaptation was implemented using eight slices, grouped into four regions, with processing distributed across four dedicated cores on the base station. This configuration was selected to balance reconstruction coverage resolution with computational efficiency, enabling near-RT operation during flight. Nevertheless, further refinements are

possible, such as dynamically adjusting the number of slices or regions based on geometry and coverage, or optimizing workload distribution to reduce processing latency.

C. Non-RT 3D Object Generation Pipeline

The open source Meshroom software from AliceVision [35] was used for implementing the non-RT 3D generation pipeline. The SfM-originating camera positions are used in addition to LPS coordinates. This is done by combining the output of the SfM and merging it with the rotated and translated Crazyflie-originating coordinates, as indicated in Figure 3. The implementation of this location-aware approach is carried out in the form of a Python script, which identifies the images used in the estimated reconstruction, retrieves the corresponding location data, and applies a coordinate transformation to merge it with the SfM-originating coordinates.

Figure 7 depicts the implementation of the N3DR-based non-RT reconstruction functionality using Nerfacto [36]. This pipeline follows a standard approach for N3DR, utilizing the default optimizations provided by the Nerfacto model. In a comparative analysis conducted in a previous study [26], we evaluated several N3DR models and found that Nerfacto consistently delivered high accuracy in 3D reconstruction.

Errors in the projected camera poses are expected, especially for mobile cameras. Misaligned stances can cause a decrease in sharpness and clarity as well as hazy artifacts. The system may back-propagate loss gradients to the input pose calculations thanks to the NeRF pipeline, particularly with the **Pose Refinement**. With this knowledge, improving and polishing the position estimates is possible.

The **Piecewise Sampler** creates the first set of scene samples. Up to a distance of one meter from the camera, this sampler evenly distributes half of the samples. Every sample that remains is distributed so that the step size increases. The frustums are scaled replicas of themselves when the step size is selected. Far-off items can be handled while maintaining a dense set of data for close-by objects by raising the step sizes. The sample locations are combined by the **Proposal Sampler** to the areas of the scene that are most important to the final render (usually the first surface intersection). This significantly raises the caliber of 3D reconstruction. The density function for the scene is needed by the proposal network sampler. There are several ways to construct the density function, but it was empirically found that the smallest fused Multilayer

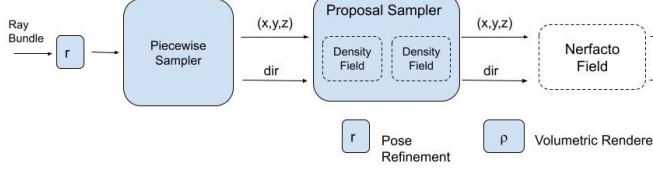


Fig. 7: Nerfacto pipeline.

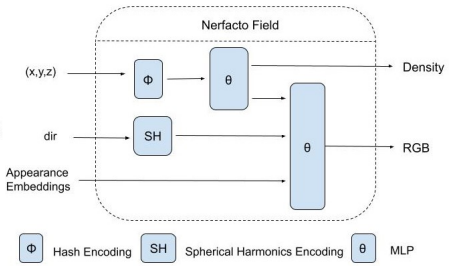


Fig. 8: Nerfacto Field specification.

Perceptron (MLP) with a hash encoding works well and quickly. The proposal network sampler can be chained together with different density functions to further consolidate the sampling. Two density functions are preferable to one [36].

To direct sampling, the **Density Field** has to depict a rough density representation of the scene. A quick technique to query the scene is to combine a tiny fused MLP from tiny-cudann with a hash encoding. We can increase its efficiency by reducing the size of the encoding dictionary and the number of feature levels. Since the density function does not have to learn high-frequency information during the initial runs, these simplifications do not significantly affect the reconstruction quality. **Nerfacto Field** is used for rendering different types of visualizations, including the NeRF-based render, pointcloud or mesh visualization, and the rendered video. Figure 8 depicts the Nerfacto Field architecture and shows that there are two types of encodings, the Hash encoding and a spherical harmonics encoding that has the direction of the ray as an input. Finally, using the positions, the appearance similarities between rays and their directions, all that input is put on the MLP to obtain the density and the images.

The density field is used to figure out if there is an object on that part of the scene, while the RGB is utilized to generate the color of that part of the scene. Once all iterations of the training are done, the overall density field and the RGB field are used to compose the NeRF visualization, that then renders new views of the scene. After generating and rendering the different views, a pointcloud is obtained by using the samples of the different rays that come from the viewpoint and pixels of each image, while a mesh is acquired as a Poisson surface reconstruction from the normals of the models [37].

V. EVALUATION METHODOLOGY

This section provides an overview of the evaluations performed to assess the 3D reconstruction performance of our system. The evaluations are based on images captured by small UAVs with location data from UWB positioning, tested under single- and multi-UAV setups with static and dynamic UAV trajectories, and using both black-and-white (BW) and RGB images. A set of heterogeneous evaluation metrics is used to assess the quality and accuracy of the reconstructions.

A. Evaluation Scenarios

The small reference object for 3D reconstruction is depicted in Figure 9a-b. The resulting 3D-printed object features the size of $54.7 \times 20.3 \times 20.9 \text{ cm}^3$, with the letters and engravings

having a depth of 4 cm. Figure 6a shows an example BW image of this object captured by the Crazyflie UAV.

To evaluate the system's scalability and robustness under more complex visual and structural conditions, we introduce a 3D-printed anatomical model of the human gastrointestinal (GI) system as a second reference object. This object, depicted in Figure 9c, is fabricated using transparent polymer, which introduces significant challenges for visual reconstruction due to light refraction and low-contrast internal features. Moreover, its anatomical shape and vertical span, featuring a height of approximately 90 cm, represent a substantial departure from the compact, high-contrast first object. This test case is used to assess the limits of both the near- and non-RT reconstruction pipelines when facing large, visually ambiguous geometries. Figure 6c depicts an example RGB image of this object.

For the static experiments, the UAVs were instructed to follow a static trajectory around the objects, maintaining an approximate distance of 50 cm from each of them. The objects were positioned at a height of approximately 1 m from the floor. Each UAV was able to complete 2-3 circles around the object, capturing approximately 250 images in the process. In the dual-UAV experiments, the UAVs were initially positioned opposing each other and followed the same static flight trajectories, with a small difference of 10 cm in their altitude during concurrent circles.

The works from the literature utilize more powerful UAVs and/or target comparably larger objects (cf., Section II), hence we were unable to use such proposals as baselines in our evaluation. The intuition of our experiments is, hence, to utilize the static experiment as the baseline, followed by introducing and evaluating the impact of both location-awareness and dynamic path adaptation as additional system functionalities.

Specifically, to establish a baseline for subsequent experiments, initial scans of the objects were conducted using a single UAV following a static trajectory. Reconstruction relied on SfM-originating estimated camera positions, providing a straightforward implementation with expedited results and representing the simplest setup in terms of implementation and computational efficiency (i.e., the **baseline approach**). To enhance the baseline, some experiments deployed a second UAV, effectively doubling the number of captured images. This configuration aimed to improve reconstruction quality, particularly in refining estimated camera positions and poses, leveraging the increased image density.

Both single and multi-UAV setups were re-evaluated by modifying the image processing pipeline to utilize camera positions and poses measured by the LPS (i.e., the **location-**

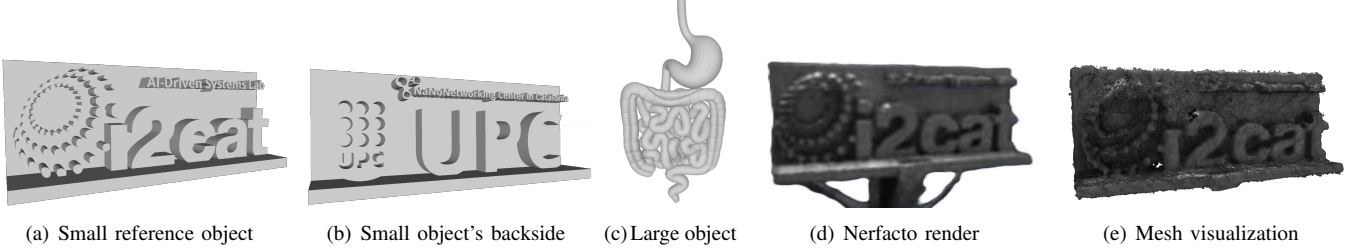


Fig. 9: Object for reconstruction and resulting visualizations

aware approach), in addition to the ones stemming from SfM. Experiments encompassed both static and dynamic trajectories. Given the wide view angle of the AI-Deck camera relative to the object’s size, dynamic trajectory results (i.e., the **dynamic path approach**) were anticipated to parallel the static ones. However, scalability considerations are expected to favor dynamic methods for superior performance in larger-scale applications. The **integrated approach** features both location-awareness through the utilization of LPS-originating locations and the dynamic trajectory adaptation.

Experiments were conducted using both BW and RGB camera input modes to evaluate the influence of color information on reconstruction fidelity. Moreover, each configuration was tested using both a near-RT pipeline and a non-RT offline NeRF-based pipeline to assess trade-offs between reconstruction quality and processing time.

The result of each experiment is the 3D reconstructed object in the form of a Nerfacto render (cf., Figure 9d), as well as mesh (cf., Figure 9e) and pointcloud visualizations. The pointclouds are used in the evaluation due to their wide utilization and consequent availability of programmatic frameworks for the calculation of the utilized performance metrics. To ensure meaningful evaluation, alignment between reconstructed pointclouds and a reference was critical. Pointcloud orientation and scaling consistency were achieved by computing scaling factors from bounding box ratios and employing fast global registration and principal component analysis for orientation correction. Alignment was refined through global registration techniques based on feature matching and iterative closest point algorithm. Post-alignment, virtual cameras were generated uniformly around the object and directed towards its center, to render images from both the reference and reconstructed pointclouds. Performance metrics were subsequently calculated directly from the pointclouds or from comparisons with the rendered images.

B. Performance Metrics

The performance metrics used to assess the quality of the pointcloud are as follows. **Peak Signal-to-Noise Ratio (PSNR)** measures the ratio between the maximum possible signal power and the noise affecting its quality [38].

Structural Similarity Index Measure (SSIM) evaluates the structural similarity between the images and the 3D render. It yields a value between -1 and 1, with 1 indicating perfect similarity and 0 indicating no similarity. The metric combines luminance, contrast, and structure comparisons across different image windows [39].

Learned Perceptual Image Patch Similarity (LPIPS) measures perceptual similarity between images and the 3D render. A value of 0 is optimal, while values approaching 1 indicate poorer similarity. This metric matches human perception closely by comparing the activations of image patches within a neural network [40].

Hausdorff Distance (HD) is the maximum distance between points in the reference and reconstructed pointclouds, indicating overall reconstruction deviation from the reference.

Wasserstein Distance (WD) calculates the minimum *work* required to transform the reconstructed pointcloud into the reference. It is effective for comparing pointclouds by considering their underlying probability distributions.

For both the single and dual-UAV setups, the **Reconstruction Latency** measures the time taken to merge a new image set with the existing pointcloud for near-RT reconstruction, reported as the mean and standard deviation. The non-RT latency in the single and dual-UAV setups refers to the total time required for NeRF training and pointcloud rendering.

In addition to reconstruction quality and latency metrics, we also report the number of images captured by the UAVs and subsequently used in each reconstruction experiment, as an indicator of trajectory coverage and system scalability.

VI. EVALUATION RESULTS

A. Reconstruction Accuracy

This set of experiments focuses exclusively on the reconstruction of the small reference object using BW images. The goal is to evaluate the impact of location-awareness (via UAV-provided camera poses) and dynamic path planning on reconstruction quality in both single- and multi-UAV configurations.

The near-RT results of our experiments are depicted in Figures 10 and 11 for single- and dual-UAV setups, respectively. Moreover, Figures 12 and 13 depict the final pointclouds of the Nerfacto-based non-RT reconstruction. The achieved results are summarized in Tables I and II for respectively single- and dual-UAV setups.

As shown in Figures 10 and 11, the near-RT reconstruction is hardly recognizable to the human eye; however, it delivers a rough shape and contours of the object, regardless of the utilized approach. This level of fidelity is sufficient for UAV control tasks such as dynamic trajectory adaptation for reconstruction quality optimization or collision avoidance with the target object. This is exemplified in the dynamic path approach, where the UAV positioning is performed in a way that optimizes the quality of the reconstructed object. This dynamic path adaptation results in consistently improved

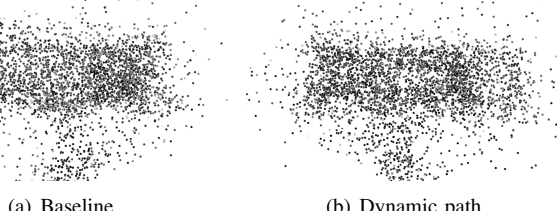


Fig. 10: Near-RT reconstruction for single-UAV setup.

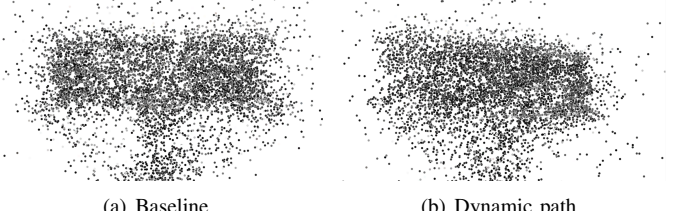
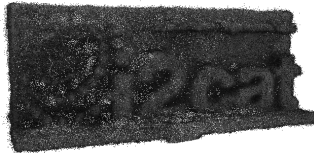


Fig. 11: Near-RT reconstruction for dual-UAV setup.



(a) Baseline



(b) Location-aware

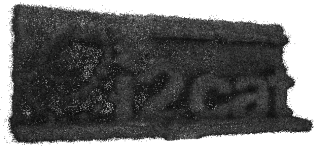


(c) Dynamic path



(d) Integrated

Fig. 12: Non-RT reconstruction for single-UAV setup.



(a) Baseline



(b) Location-aware



(c) Dynamic path



(d) Integrated

Fig. 13: Non-RT reconstruction for dual-UAV setup.

TABLE I: Single-UAV system-based 3D reconstruction results demonstrating the advantages of location-aware 3D reconstruction and dynamic UAV trajectory adaptation based on instantaneous pointcloud quality.

Approach	PSNR [dB]	SSIM	LPIPS	HD	WD	Latency [sec]	# images taken	# images used
Near-real-time 3D reconstruction								
Baseline	3.295	0.888 ± 0.025	0.2490 ± 0.039	0.6324	0.0249	23.044 ± 9.04	233	232
Dynamic path	4.095	0.886 ± 0.027	0.2764 ± 0.053	0.5733	0.0275	23.648 ± 9.99	271	266
Non-real-time 3D reconstruction								
Baseline	7.720	0.961 ± 0.006	0.0429 ± 0.008	0.0686	0.0208	224	233	232
Location-aware	7.817	0.962 ± 0.007	0.0408 ± 0.007	0.0668	0.0219	237	233	233
Dynamic path	7.639	0.961 ± 0.008	0.0419 ± 0.008	0.0742	0.0215	240	271	271
Integrated	7.723	0.962 ± 0.005	0.0411 ± 0.007	0.0726	0.0207	257	271	271

TABLE II: Dual-UAV system-based 3D reconstruction results demonstrating the advantages of location-aware 3D reconstruction and dynamic UAV trajectory adaptation based on instantaneous pointcloud quality.

Approach	PSNR [dB]	SSIM	LPIPS	HD	WD	Latency [sec]	# images taken	# images used
Near-real-time 3D reconstruction								
Baseline	4.651	0.901 ± 0.018	0.2255 ± 0.028	0.3991	0.0240	34.756 ± 21.14	466	461
Dynamic path	5.624	0.927 ± 0.009	0.1572 ± 0.018	0.3447	0.0239	31.225 ± 13.16	507	501
Non-real-time 3D reconstruction								
Baseline	7.651	0.963 ± 0.006	0.0397 ± 0.007	0.0686	0.0219	222	466	465
Location-aware	7.695	0.965 ± 0.007	0.0375 ± 0.006	0.0704	0.0210	217	466	466
Dynamic path	7.704	0.963 ± 0.006	0.0404 ± 0.008	0.0685	0.0227	232	507	507
Integrated	7.561	0.964 ± 0.005	0.0390 ± 0.008	0.0725	0.0226	226	507	507

quality of near-RT reconstruction for both single- and dual-UAV setups, as shown in Tables I and II. For example, the improvement in the PSNR of reconstruction due to the dynamic path adaptation is around 1 dB for both setups.

As shown in Figures 12 and 13, the utilization of location-awareness in the form of both leveraging UAV-originating camera locations in non-RT reconstruction and dynamic UAV

trajectory adaptation improves the quality of reconstruction. Specifically, the location-aware approach increases the reliability of the pointcloud generation as it provides an additional source of camera locations. In other words, obtaining coordinates utilizing SfM is possible only if the aligned images have sufficient features for camera localization, while in the location-aware approach the UAV can be utilized as

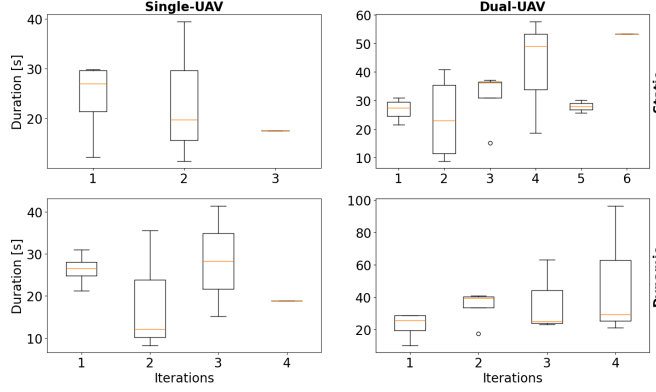


Fig. 14: Near-RT reconstruction latency.

a substitute. This eventually results in the larger number of images used by the N3DR approach for reconstruction. Tables I and II show this effect, where the location-aware and integrated approaches always use all images taken by the UAVs for reconstruction.

In addition, the dynamic path approach does not degrade the performance of non-RT reconstruction compared to the baseline, although its primary optimization objective is the near-RT reconstruction accuracy. Finally, the integrated approach combining both location-aware reconstruction and dynamic UAV trajectory adaptation demonstrates improved reconstruction accuracy and consistently outperforms the baseline, as reflected in the higher SSIM and lower HD values in both single- and dual-UAV setups. These experiments show that location-awareness and dynamic path adaptation are valuable tools to enhance performance without added hardware complexity.

B. Reconstruction Latency

A reconstruction iteration refers to the process of updating the 3D pointcloud based on the newly acquired images from the UAV. In our approach, new reconstruction iterations are triggered in two cases. First, if the UAV exits a section, all images captured in that section are added to the reconstructed pointcloud (typically 45 images). These images are processed in a new iteration of the 3D reconstruction pipeline to update the pointcloud. Second, a new reconstruction iteration is triggered if the elapsed time between capturing two images exceeds a predefined time threshold. The second condition improves efficiency by triggering a reconstruction process while the UAV is moving to a new position. This was particularly necessary in cases where the movement takes longer due to a farther set-point (in the case of dynamic trajectory) or due to imprecise position estimation with the LPS. A reconstruction triggered by the second condition processes fewer images (as few as 2), which reduces processing time but leads to inconsistencies in near-RT latency measurements, as shown in Figure 14. From these measurements, we conclude that while the baseline latency was lower for single-UAV experiments (due to the smaller number of images used), in the dual-UAV setup, the dynamic trajectory and the need for both UAVs to arrive at the set-point resulted in more frequent triggering of the reconstruction process, leading to lower latency despite the higher number of images used.

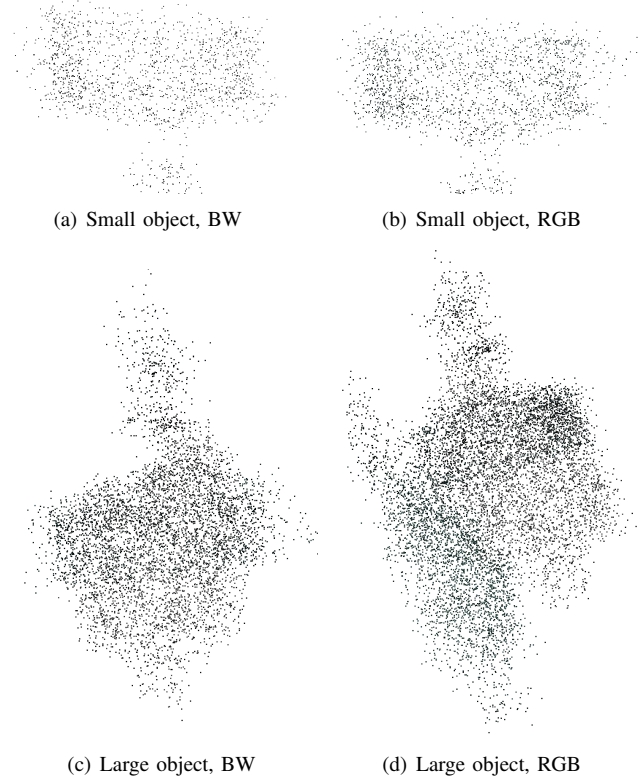


Fig. 15: SfM pointclouds for different camera types and objects.

Investigating the non-RT reconstruction latencies in Tables I and II shows that the reconstruction with the dual-UAV setup is generally faster than the single-UAV counterpart. This might be considered counterintuitive, given that the latency is expected to increase with the number of images. The shorter reconstruction latency can be explained because more images provided to Nerfacto result in fewer iterations needed for the reconstruction. In contrast, the latency increases with the number of captured images in both single and dual setups, causing the dynamic path and integrated approaches to be slightly slower. The reason for that is that the number of iterations was kept constant to guarantee objective comparison when considering different approaches in each UAV setup.

C. Reconstruction Scalability

To evaluate the scalability and robustness of the proposed pipeline, we extend our experiments beyond the original small object by introducing a significantly more complex and larger anatomical test case. We conduct reconstructions of both objects using BW and RGB image inputs captured with a single-UAV configuration. The corresponding SfM pointclouds and Nerfacto renders are presented in Figures 15 and 16, respectively. Table III summarizes the quantitative evaluation results for all configurations. The results are derived for the integrated approach, given its superior performance in the previous experiments.

The results highlight that the pipeline scales effectively with both visually and structurally complex targets. For the small object, BW reconstructions perform slightly better than RGB across both near- and non-RT pipelines. BW achieves higher

TABLE III: Single-UAV system-based 3D reconstruction results for different camera types and objects.

Object, Camera Type	PSNR [dB]	SSIM	LPIPS	HD	WD	# images taken	# images used
Near-real-time 3D reconstruction							
Small Object, BW	7.859	0.971 ± 0.018	0.0549 ± 0.0075	0.126	0.026	291	291
Small Object, RGB	6.851	0.968 ± 0.014	0.0644 ± 0.0092	0.127	0.031	302	302
Large Object, BW	14.339	0.929 ± 0.021	0.0694 ± 0.0369	182.360	17.38	283	283
Large Object, RGB	14.770	0.958 ± 0.022	0.0763 ± 0.0422	114.370	32.62	265	265
Non-real-time 3D reconstruction							
Small Object, BW	7.566	0.984 ± 0.0056	0.0483 ± 0.0078	0.110	0.025	291	291
Small Object, RGB	7.541	0.978 ± 0.0066	0.0523 ± 0.0087	0.112	0.028	302	302
Large Object, BW	15.668	0.949 ± 0.0226	0.0667 ± 0.0357	129.036	26.88	283	283
Large Object, RGB	16.133	0.986 ± 0.0192	0.0499 ± 0.0236	95.230	30.43	265	265

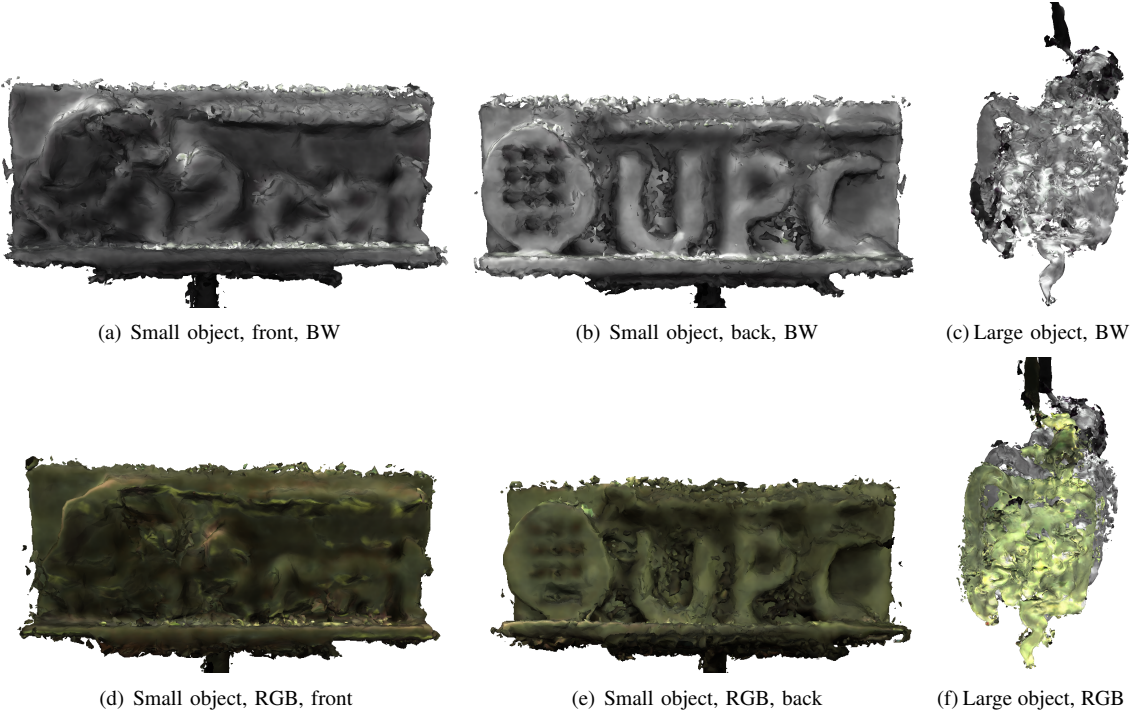


Fig. 16: Nerfacto renders for different camera types and objects.

SSIM (0.971 vs. 0.968 in near-RT, 0.984 vs. 0.978 in non-RT) and nearly identical HD values (0.126–0.127 near-RT, 0.110–0.112 non-RT), indicating marginally stronger structural similarity and geometric accuracy.

For the large object, the trend reverses, with RGB consistently outperforming BW. In both near- and non-RT reconstructions, RGB achieves higher SSIM (0.958 vs. 0.929 in near-RT, 0.986 vs. 0.949 in non-RT) and lower HD (95.23 vs. 182.36 in near-RT, 95.23 vs. 129.04 in non-RT). This demonstrates that RGB cameras capture structural similarity more effectively while also reducing geometric deviations, particularly for complex or reflective objects where richer visual cues are necessary for stable reconstruction.

This tradeoff illustrates that image modality selection should consider both the object’s material and structural complexity. While BW images perform slightly better for compact, opaque objects, RGB images provide superior results for larger or reflective objects. These findings further validate the adaptability of our reconstruction framework across varied scenarios and underline the importance of location-aware modality selection in autonomous UAV-based scanning systems.

VII. DISCUSSION AND FUTURE EFFORTS

Several areas for improvement emerge from our findings. First, the dimensioning of the number of UAVs in a particular deployment setup should be based on the target object’s size for optimizing coverage and resolution. Future efforts should focus on refining these dimensions to accommodate larger objects and improving the latency of near-RT reconstruction. Evaluations should be expanded to assess the feasibility and performance of our system on a larger scale.

Second, standardizing an evaluation framework as the target reconstruction objects become smaller and more detailed will be essential for objectively comparing and benchmarking different systems and approaches in UAV-based 3D reconstruction. This framework should encompass metrics for accuracy, efficiency, scalability, and usability, ensuring comprehensive assessments across diverse applications and environments. The capability of the framework in accurately capturing the performance trends and intricate differences between reconstructions should be assessed to showcase the ability of the selected reconstruction accuracy metrics to capture the inherent limits of different reconstruction approaches.

These experiments also reveal the sensitivity of reconstruction performance to camera modality and object properties. While RGB images generally yield denser pointclouds, they may introduce more artifacts in the presence of surface reflections, as observed with the larger object. In contrast, BW images, although producing sparser pointclouds, achieved more accurate reconstructions in such scenarios. This suggests that future system designs should consider adaptive camera modality selection based on real-time scene analysis, e.g., preferring BW sensors for reflective or complex geometries and RGB for small, high-contrast objects.

From the system's perspective, introducing RGB cameras and integrating features like obstacle avoidance based on near-RT reconstruction capabilities could enhance the capabilities of our prototype. These advancements would improve sensing capabilities and expand the range of applications, particularly in complex and dynamic environments where real-time decision-making and obstacle detection are crucial. Enhancing the reliability of UAV operations is also paramount. This includes an often overlooked issue of degradation in the performance of Radio Frequency (RF)-based localization, such as the UWB system utilized in this work, due to RF interference [41], [42], which caused substantial hurdles in terms of UAV control in the deployment environment. Moreover, enhancing electronic components' reliability and optimizing system-level performance will be essential for ensuring robust and consistent performance across operational scenarios.

Adaptations of our UAV setup to leverage high-frequency Joint Communications and Sensing (JCAS) paradigms [43]–[45] for communication, 3D imaging, and UAV localization and control would open new avenues for 3D reconstruction of objects in dynamic and uncontrolled environments, as well as prolonged UAV flight duration due to lower energy consumption of the system.

Exploring advanced volumetric rendering techniques such as GS and instant-*ngp*, as well as their optimal hyperparameterizations could further improve the performance. Our initial attempt at the utilization of Splatfacto implementation of GS is promising [26], yet a reduction in its implementation's complexity is needed for wider-scale deployments. These approaches offer enhancements in accuracy, detail preservation, and computational efficiency, thus advancing small UAV-based 3D reconstruction. They will serve as an enabler of additional applications such as 3D anomaly detection.

VIII. CONCLUSION

We have presented a novel system architecture for utilizing small UAVs to autonomously generate high-resolution 3D digital representations of small static objects. Our implemented system harnesses the capabilities of small Crazyflie UAVs as carriers and power sources for camera sensors, enabling them to capture images from multiple vantage points around the object of interest. These images are transmitted to a base station executing an open-source pipeline for near-RT and non-RT 3D object reconstruction.

We have experimentally demonstrated encouraging reconstruction performance of the setup for single and multi-UAV

deployments, and for small and large objects. Our results demonstrate that context-awareness via accurate UWB-based camera localization and dynamic path planning consistently improve reconstruction quality. We further investigate the system's scalability to larger and more complex objects, showing that performance varies with camera modality and object properties, emphasizing the importance of context-aware reconstruction strategies.

While our system represents an advancement in small UAV-based 3D reconstruction, ongoing research and development efforts will be crucial for unlocking the full potential of small UAVs in fine-grained photogrammetry, digital mapping, anomaly detection, and environmental monitoring.

ACKNOWLEDGMENTS

This work was supported by the European Union's Horizon Europe's programme (grants n° 101139161 - INSTINCT and n° 101192521 - MultiX projects).

REFERENCES

- [1] M. Mozaffari, X. Lin, and S. Hayes, "Toward 6g with connected sky: Uavs and beyond," *IEEE Communications Magazine*, vol. 59, no. 12, pp. 74–80, 2021.
- [2] B. Rinner, C. Bettstetter, H. Hellwagner, and S. Weiss, "Multidrone systems: More than the sum of the parts," *Computer*, vol. 54, no. 5, pp. 34–43, 2021.
- [3] D. Floreano *et al.*, "Science, technology and the future of small autonomous drones," *Nature*, vol. 521, no. 7553, pp. 460–466, 2015.
- [4] M. Gordan, Z. Ismail, K. Ghaedi, Z. Ibrahim, H. Hashim, H. H. Ghayeb, and M. Talebkhan, "A brief overview and future perspective of unmanned aerial systems for in-service structural health monitoring," *Engineering Advances*, vol. 1, no. 1, pp. 9–15, 2021.
- [5] P. Talarin, B. Ollé, F. Lemic, S. Abadal, and X. Costa-Perez, "Real-time generation of 3-dimensional representations of static objects using small unmanned aerial vehicles," in *Proc. ACM Mobile Computing and Networking (MobiCom)*, 2023, pp. 1–3.
- [6] X. Liu, S. W. Chen, G. V. Nardari, C. Qu, F. Cladera, *et al.*, "Challenges and opportunities for autonomous micro-uavs in precision agriculture," *IEEE Micro*, vol. 42, no. 1, pp. 61–68, 2022.
- [7] S. Campana, "Drones in archaeology. sota and future perspectives," *Archaeological Prospection*, vol. 24, no. 4, pp. 275–296, 2017.
- [8] D. Giordan, M. S. Adams, I. Aicardi, *et al.*, "The use of uavs for engineering geology applications," *Bulletin of Engineering Geology and the Environment*, vol. 79, pp. 3437–3481, 2020.
- [9] S. A. H. Mohsan, N. Q. H. Othman, Y. Li, M. H. Alsharif, and M. A. Khan, "Unmanned aerial vehicles (uavs): Practical aspects, applications, open challenges, security issues, and future trends," *Intelligent Service Robotics*, vol. 16, no. 1, pp. 109–137, 2023.
- [10] E. K. Stathopoulou, M. Welponer, and F. Remondino, "Open-source image-based 3d reconstruction pipelines: Review, comparison and evaluation," *Photogrammetry, Remote Sensing and Spatial Information Sciences, Volume XLII-2/W17*, pp. 331–338, 2019.
- [11] D. Mourtzis, J. Angelopoulos, and N. Panopoulos, "Uavs for industrial applications: Identifying challenges and opportunities from the implementation point of view," *Procedia Manufacturing*, vol. 55, pp. 183–190, 2021.
- [12] F. Yan, E. Xia, Z. Li, and Z. Zhou, "Sampling-based path planning for high-quality aerial 3d reconstruction of urban scenes," *Remote Sensing*, vol. 13, no. 5, p. 989, 2021.
- [13] S. Karam, F. Nex, O. Karlsson, J. Rydell, E. Bilock, M. Tull Dahl, M. Holmberg, and N. Kerle, "Micro and macro quadcopter drones for indoor mapping to support disaster management," *ISPRS Annals of the Photogrammetry, Remote Sensing and Spatial Information Sciences*, vol. 1, pp. 203–210, 2022.
- [14] L. Wawrla, O. Maghazei, and T. Netland, "Applications of drones in warehouse operations," Whitepaper. ETH Zurich, D-MTEC, Tech. Rep., 2019, pp. 1–12.
- [15] P. De Petris, H. Nguyen, M. Dharmadhikari, *et al.*, "Rmf-owl: A collision-tolerant flying robot for autonomous subterranean exploration," in *Proc. International Conference on Unmanned Aircraft Systems (ICUAS)*, IEEE, 2022, pp. 536–543.

[16] Z. Xu, L. Wu, M. Gerke, R. Wang, and H. Yang, “Skeletal camera network embedded structure-from-motion for 3d scene reconstruction from uav images,” *ISPRS Photogrammetry and Remote Sensing*, vol. 121, pp. 113–127, 2016.

[17] M. Maboudi, M. Homaei, S. Song, S. Malihi, M. Saadatseresht, and M. Gerke, “A review on viewpoints and path planning for uav-based 3d reconstruction,” *IEEE Journal of Selected Topics in Applied Earth Observations and Remote Sensing*, vol. 16, pp. 5026–5048, 2023.

[18] T. Schenk, “Introduction to photogrammetry,” The Ohio State University, Columbus, Tech. Rep., 2005.

[19] L. Kovanič, B. Topitzer, P. Petovský, P. Blíštan, M. B. Gergelová, and M. Blíštanová, “Review of photogrammetric and lidar applications of uav,” *Applied Sciences*, vol. 13, no. 11, p. 6732, 2023.

[20] P. Kamencay, M. Breznan, R. Jarina, P. Lukac, and M. Zachariasova, “Improved depth map estimation from stereo images based on hybrid method,” *Radioengineering*, vol. 21, no. 1, 2012.

[21] B. Mildenhall, P. P. Srinivasan, M. Tancik, J. T. Barron, R. Ramamoorthi, and R. Ng, “Nerf: Representing scenes as neural radiance fields for view synthesis,” *Communications of the ACM*, vol. 65, no. 1, pp. 99–106, 2021.

[22] K. Gao, Y. Gao, H. He, D. Lu, L. Xu, and J. Li, “Nerf: Neural radiance field in 3d vision: A comprehensive review,” *arXiv preprint arXiv:2210.00379*, 2022.

[23] B. Kerbl, G. Kopanas, T. Leimkühler, and G. Drettakis, “3d gaussian splatting for real-time radiance field rendering,” *ACM Transactions on Graphics*, vol. 42, no. 4, pp. 1–14, 2023.

[24] T. Müller, A. Evans, C. Schied, and A. Keller, “Instant neural graphics primitives with a multiresolution hash encoding,” *ACM Transactions on Graphics*, vol. 41, no. 4, pp. 1–15, 2022.

[25] X. Zhang, P. P. Srinivasan, B. Deng, P. Debevec, W. T. Freeman, and J. T. Barron, “Nerfactor: Neural factorization of shape and reflectance under an unknown illumination,” *ACM Transactions on Graphics*, vol. 40, no. 6, pp. 1–18, 2021.

[26] G. C. Gómez-Raya, Á. Veres-Vitályos, F. Lemic, P. Royo, M. Montagud, S. Fernández, S. Abadal, and X. Costa-Pérez, “Experimental assessment of neural 3d reconstruction for small uav-based applications,” in *Proc. IEEE International Symposium on Personal, Indoor and Mobile Radio Communications (PIMRC)*, 2025.

[27] H. Matsuki, R. Murai, P. H. Kelly, and A. J. Davison, “Gaussian splatting slam,” in *Proc. IEEE/CVF Conference on Computer Vision and Pattern Recognition*, 2024, pp. 18039–18048.

[28] A. Rovira-Sugranes, A. Razi, F. Afghah, and J. Chakareski, “A review of ai-enabled routing protocols for uav networks: Trends, challenges, and future outlook,” *Ad Hoc Networks*, vol. 130, p. 102790, 2022.

[29] J. Liénard, A. Vogs, D. Gatziolis, and N. Strigul, “Embedded, real-time uav control for improved, image-based 3d scene reconstruction,” *Measurement*, vol. 81, pp. 264–269, 2016.

[30] T. Koch, M. Körner, and F. Fraundorfer, “Automatic and semantically-aware 3d uav flight planning for image-based 3d reconstruction,” *Remote Sensing*, vol. 11, no. 13, p. 1550, 2019.

[31] S. Krul, C. Pantos, M. Frangulea, and J. Valente, “Visual slam for indoor livestock and farming using a small drone with a monocular camera: A feasibility study,” *Drones*, vol. 5, no. 2, p. 41, 2021.

[32] F. Huang, H. Yang, X. Tan, S. Peng, J. Tao, and S. Peng, “Fast reconstruction of 3d point cloud model using visual slam on embedded uav development platform,” *Remote Sensing*, vol. 12, no. 20, p. 3308, 2020.

[33] C. Gao, X. Wang, R. Wang, Z. Zhao, Y. Zhai, X. Chen, and B. M. Chen, “A uav-based explore-then-exploit system for autonomous indoor facility inspection and scene reconstruction,” *Automation in Construction*, vol. 148, p. 104753, 2023.

[34] O. Özyesil, V. Voroninski, R. Basri, and A. Singer, “A survey of structure from motion,” *Acta Numerica*, vol. 26, pp. 305–364, 2017.

[35] C. Griwodz, S. Gasparini, L. Calvet, P. Gurdjos, F. Castan, B. Maujean, G. D. Lillo, and Y. Lanthony, “Alicevision Meshroom: An open-source 3D reconstruction pipeline,” in *Proc. ACM Multimedia Systems Conference (MMSys’21)*, ACM Press, 2021.

[36] M. Tancik, E. Weber, E. Ng, *et al.*, “Nerfstudio: A modular framework for neural radiance field development,” in *Proc. ACM Special Interest Group on Computer Graphics (SIGGRAPH)*, 2023, pp. 1–12.

[37] M. Kazhdan, M. Bolitho, and H. Hoppe, “Poisson surface reconstruction,” in *Proc. Eurographics Symposium on Geometry Processing*, vol. 7, 2006.

[38] A. Hore and D. Ziou, “Image quality metrics: Psnr vs. ssim,” in *Proc. IEEE International Conference on Pattern Recognition*, 2010, pp. 2366–2369.

[39] Z. Wang, E. P. Simoncelli, and A. C. Bovik, “Multiscale structural similarity for image quality assessment,” in *Proc. Asilomar Conference on Signals, Systems & Computers*, IEEE, vol. 2, 2003, pp. 1398–1402.

[40] R. Zhang, P. Isola, A. Efros, *et al.*, “The unreasonable effectiveness of deep features as a perceptual metric,” in *Proc. IEEE/CVF Conference on Computer Vision and Pattern Recognition*, 2018, pp. 586–595.

[41] A. Behboodi, N. Wirstrom, *et al.*, “Interference effect on localization solutions: Signal feature perspective,” in *Proc. IEEE Vehicular Technology Conference (VTC Spring)*, IEEE, 2015, pp. 1–7.

[42] F. Lemic, V. Handziski, A. Wolisz, T. Constambeys, C. Laoudias, S. Adler, S. Schmitt, and Y. Yang, “Experimental evaluation of rf-based indoor localization algorithms under rf interference,” in *Proc. International Conference on Localization and GNSS (ICL-GNSS)*, IEEE, 2015, pp. 1–8.

[43] Y. Wu, F. Lemic, C. Han, and Z. Chen, “Sensing integrated dft-spread ofdm waveform and deep learning-powered receiver design for terahertz integrated sensing and communication systems,” *IEEE Transactions on Communications*, vol. 71, no. 1, pp. 595–610, 2022.

[44] F. Lemic, S. Abadal, W. Tavernier, *et al.*, “Survey on terahertz nanocommunication and networking: A top-down perspective,” *IEEE Journal on Selected Areas in Communications*, vol. 39, no. 6, pp. 1506–1543, 2021.

[45] C. Han, Y. Wu, Z. Chen, Y. Chen, and G. Wang, “THz ISAC: A physical-layer perspective of terahertz integrated sensing and communication,” *IEEE Communications Magazine*, vol. 62, no. 2, pp. 102–108, 2024.